Failure characterisation of sandwich beams using integrated acoustic emission and digital image correlation techniques

Łukasz Pyrzowski [a],[*], Magdalena Knak [a], Magdalena Rucka [a],[b]

[a] *Department of Mechanics of Materials and Structures, Faculty of Civil and Environmental Engineering, Gdańsk University of Technology, Narutowicza 11/12, 80-233 Gdańsk, Poland*
[b] *EkoTech Center, Gdańsk University of Technology, Narutowicza 11/12, 80-233 Gdańsk, Poland*

ARTICLE INFO

ABSTRACT

The paper presents the experimental study of the failure behaviour of sandwich beams subjected to bending. The samples examined are sandwich beams made of polyethylene terephthalate foam core and glass fibre-reinforced polymer laminate face sheets. In a series of experiments, it has been proposed to integrate diagnostic techniques with acoustic emission and digital image correlation to accurately track the cracking process on the surface as well as in the entire volume of the beam. The research programme carried out allowed observing various modes of failure in composite specimens. The results obtained showed that the integration of acoustic and optical diagnostic techniques provided complementary results and can be used successfully for failure monitoring in sandwich beams.

1. Introduction

The concept of a light composite sandwich structure, which consists of rigid face sheets and a lightweight core, was introduced in the aircraft, ship, and automobile industries in the early 20th century. Sandwich panels made of metal or increasingly fibre-reinforced plastics (FRP) are now being used in many different structural applications. Its popularity is due to specific characteristics, which are: high bending stiffness, strength combined with low weight, as well as durability including fatigue and corrosion resistance. This type of structures of have also gained popularity during recent decades in the usually conservative civil engineering industry. Currently, they are used mainly in bridge applications as decks [1–4] or as a complete structural system [5,6], but also in general building constructions such as floors [7], roofs [8] or cladding walls [9].

Lightweight sandwich structures offer designers new opportunities. Therefore, there is great interest in them among researchers. In the past three decades, a large number of experimental, analytical, and numerical studies have been done on sandwich beams or panels. The common loading case/condition of a sandwich structure is bending, so the largest amount of research completed was performed under three- or four-point bending conditions. Their main purpose was to identify the flexural properties, strength, and failure mechanisms. The most common failure

modes in these tests were buckling of an upper face sheet, debonding between a face sheet and a core, foam shear, or local damage to a face sheet under concentrated force. The following research can be given as examples. Fam and Sharaf [10] explored the feasibility of the fabrication and assessment of the flexural performance of panels made up of foam core and GFRP skins. They conducted a comprehensive material testing programme and large-scale panel bending tests with various configurations of internal and exterior GFRP ribs. Islam and Aravinthan [11] developed an innovative sandwich panel made of glass fibre-reinforced polymer skins and modified phenolic core material. Their research programme included tests of sandwich panels with different fibre orientations under point load and uniformly distributed load to determine their strength and failure mechanisms. Kulpa and Siwowski [12] proposed a composite FRP bridge deck designed for application on road bridges. They subjected the prototype full-size bridge deck to a series of static load tests that simulate the relevant load. Bahabadi et al. [13] investigated experimentally and numerically the resistance to separation between composite skins and different complex geometries of the corrugated core filled with PVC foam. Mei et al. [14] proposed foam-filled composite sandwich panels with X-core. They studied the flexural behaviours of empty and hybrid composite sandwich panels using three-point bending tests. Xie et al. [15] studied the flexural properties of polyethylene terephthalate (PET) composite sandwich panels filled

---

with foam subjected to four-point bending. They analysed the effects of different thicknesses of the face sheet and core on their flexural properties. The studies of other researchers can also be found here [16–21].

All of the above examples include the damage process of the tested structures in their scope. The studies are based mainly on observations, results from testing machines, and point measurements, such as e.g. strain gauges, and are often supported by numerical analysis. All this is done in order to better understand the processes that take place inside a structure. Recently, non-destructive testing (NDT) techniques have been greatly developed. They can often enrich and help to understand the work of a structure and can also help predict impending failure. One such technique is digital image correlation (DIC), which is based on optical principles. Until now, it has still been rarely used in the research of sandwich structures, although, the application of DIC to polymeric materials has been shown to be a powerful tool for non-contact strain measurement [22]. Nevertheless, a few examples of the application of this technique can be found. Fathi et al. [23] investigated the shear deformations of three common structural core materials: PET foam, PVC foam and Balsa wood with the aid of full-field optical analysis. Ramakrishnan et al. [24] studied parabolic impact with different trajectories on sandwich plates with Kevlar face sheets and Rohacell foam core. They measured components of the force–time history using a triaxial load cell and strain history obtained from the DIC of high-speed camera images. Sayahlatifi et al. [25] investigated the effect of the insertion of a corrugated composite into the typical balsa core sandwich structure under four-point bending. They used the DIC technique to obtain full-field strains and deflection distribution.

Another non-destructive testing technique that is already established but is still gaining popularity is acoustic emission (AE). It is a passive technique that makes use of the high-frequency acoustic energy emitted by an object. The use of this method can be observed quite often in the monitoring of FRP laminates. Many researchers use the acoustic emission technique to identify microscopic damage mechanisms, assess failure progress, identify damage modes, observe the evolution of degradation due to fatigue, or determine the position of a crack tip during propagation. Examples of such applications can be seen in [26–35]. This technique is much less often used in sandwich structures, but some examples can still be given. Pashmforoush et al. [36] used the AE technique to monitor the mode I delamination test of sandwich composites. Sikdar et al. [37] performed a coordinated semi-analytical, finite element, and experimental analysis of damage-induced AE wave propagation and source monitoring in a honeycomb sandwich composite structure. Abdulaziz et al. [38] studied AE wave propagation in a glass fibre aluminium honeycomb sandwich panel. They analysed the propagation of AE through thickness from one face sheet to the other. Rishikesan et al. [39] investigated the effects of various acoustic emission signals together with force, torque, and tool wear on the delamination caused by the honeycomb GFRP sandwich composite during the drilling process. Wu et al. [40] focused on the rapid determination of AE wave propagation velocity in composite laminate and sandwich structures using a closed-form formula to improve damage localization.

Monitoring the propagation of damage and in sandwich structures remains a challenge. The weakest element of these structures, the core hidden under rigid face sheets, is the most common cause of their failure. This paper deals with the application of acoustic emission and digital image correlation techniques for failure characterisation in composite beams subjected to bending. A set of carefully planned experiments was conducted on sandwich beams in a way that resulted in different modes of failure. The applied diagnostic techniques allowed one not only to observe what was happening with the tested sandwich beams on their surfaces, but also to enter their structure. The DIC technique allowed to observe mainly the work of the core, while the AE allowed to classify stages of damage. The main contribution of the work is the integration of two diagnostic techniques (i.e., acoustic emission and digital image correlation) to enhance quantitative damage assessment during the process of mechanical degradation. A detailed characterisation of particular stages of the fracture process was conducted by both techniques. The results showed that the two integrated diagnostic techniques allowed more accurate observations of the bending process as well as classification of damage stages.

2. Materials and methods

2.1. Specimens

The tested samples were sandwich beams of cross-section dimensions 40×74 mm^2 and length 350 mm; see Fig. 1. Their structure was made of a polyethylene terephthalate (PET) foam core and glass fibre-reinforced polymer (GFRP) laminate face sheets.

In this paper four samples were studied. Two of them (Beams #1-SD and #2-SI) were made with a PET core density of 80 kg/m^3, while the other two (Beams #3-HD and #4-HI) a core density of 200 kg/m^3. This made it possible to observe the failure process for two very different materials: 'soft' foam (80 kg/m^3) and 'hard' foam (200 kg/m^3). The material parameters of the 'soft' foam are: elastic modulus $E = 40$ MPa, shear modulus $G = 15$ MPa, compressive strength $\sigma_m = 1.02$ MPa, strain corresponding to compressive strength $\varepsilon_m = 5.9\%$, strain in the conventional elastic zone $\varepsilon_e = 1.8\%$, and of the 'hard' foam are: elastic modulus $E = 148$ MPa, shear modulus $G = 50$ MPa, compressive strength $\sigma_m = 3.99$ MPa, strain corresponding to compressive strength $\varepsilon_m = 5.3\%$, strain in the conventional elastic zone $\varepsilon_e = 2.0\%$ [41]. In both cases, the identification was carried out according to the ISO 844:2021 standard. All four samples had the same face sheets made of a GFRP laminate. Each laminate consisted of vinylester resin and quasi-balanced knitted glass fibre fabrics of 800 g/m^2 in the following sequence [0/90/+45/ −45]$_s$. Its mechanical properties are: the equivalent elastic modulus $E = 18.4$ GPa and strength $f_t = 290$ MPa.

The samples were manufactured using a vacuum infusion process. First, sandwich plates were made, and then they were appropriately cut into beams. Manufacturing with this technology ensures a high-quality product; however, the technological requirements force certain treatments. To ensure the flow of resin between face sheets, a core has to be perforated. This is usually done by drilling a hole pattern, and this was also done for the analysed material. Therefore, additional pure resin columns with a 3 mm diameter and height the same as the core height, were formed during manufacturing. They can be seen in Fig. 1 as dark spots on the laminate surface. The hole pattern in the 80 kg/m^3 core was 70 mm, while the 200 kg/m^3 core was 50 mm. It is also worth mentioning that PET foam is not exactly an isotropic material. Its manufacturing process involves the production of plates which are further welded to blocks and then sliced to dimensions given by a customer. The welding surfaces perpendicular to the length of the beam are marked with arrows in Fig. 1. The denser the foam, the closer the welded surfaces are to each other.

2.2. Experimental setup and procedure

The prepared beams were subjected to the three-point bending test. The experiments were carried out using the Zwick/Roell Z10 Universal Testing Machine (UTM) with the flexure test kit. The device consisted of two steel supports with a 5 mm radius rounding and an upper centrally placed punch also with a 5 mm radius rounding to apply a load. The support spacing was assumed to be 250 mm. The beams were first preloaded with a force of 10 N and then further loaded until failure with a cross-head displacement rate of 2 mm/min. During the test, two load application methods were used: a concentrated line force induced directly by the punch hereinafter called 'line load' (Beams #1-SD, #3-HD) and a force induced by the use of an additional plate of 30×40 mm^2 surface dimensions and 4 mm thickness, hereinafter called 'surface load' (Beams #2-SI, #4-HI); see Fig. 2. Two methods were applied to analyse a very unfavourable scheme for sandwich structures, which is a concentrated force and a much more favourable scheme, which is a force
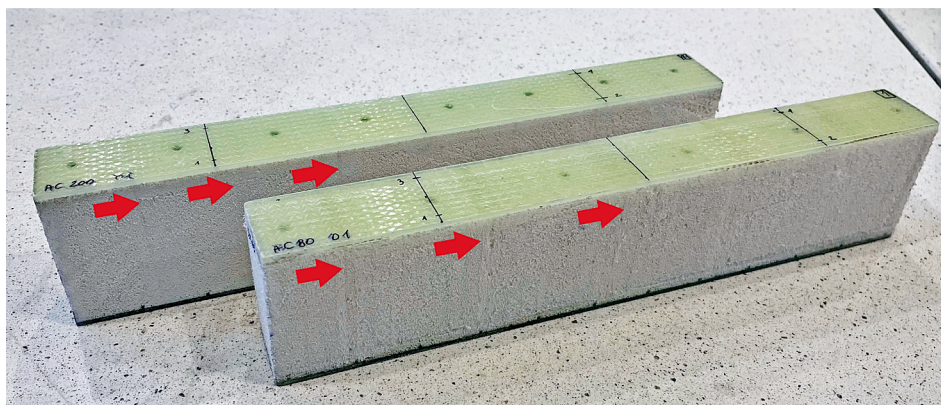
Fig. 1. Beams prepared for testing: 80 kg/m^3 core (front) and 200 kg/m^3 core (rear).
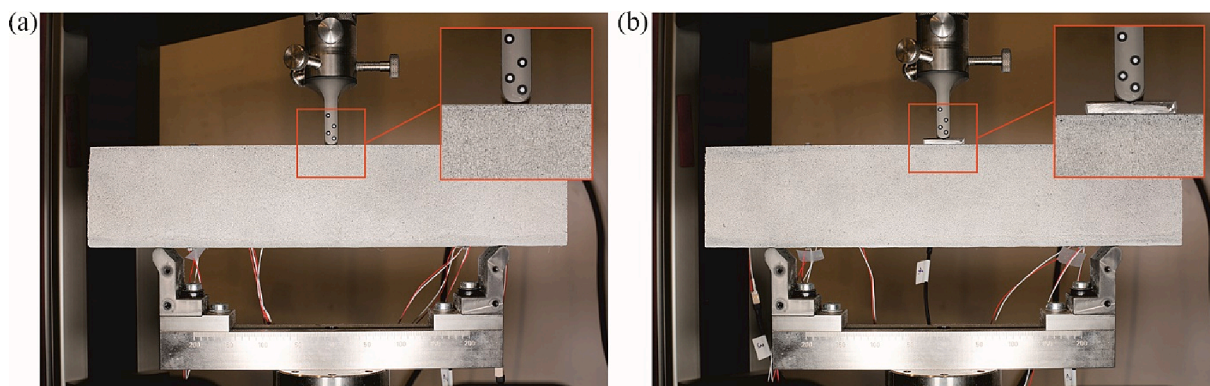

Fig. 2. Beam loaded by: (a) line load (Beams #1-SD, #3-HD) (b) surface load (Beams #2-SI, #4-HI).

distributed over a surface. The goal was to get different failure modes.

The beam failure was monitored by two independent systems based on the Acoustic Emission and Digital Image Correlation techniques; see Fig. 3a. Sensors used in AE were multilayer piezoelectric transducers NAC2024 (Noliac). In total, eight transducers (Sensors S1 ÷ S8) were used, located as shown in Fig. 3b. Data acquisition was carried out using
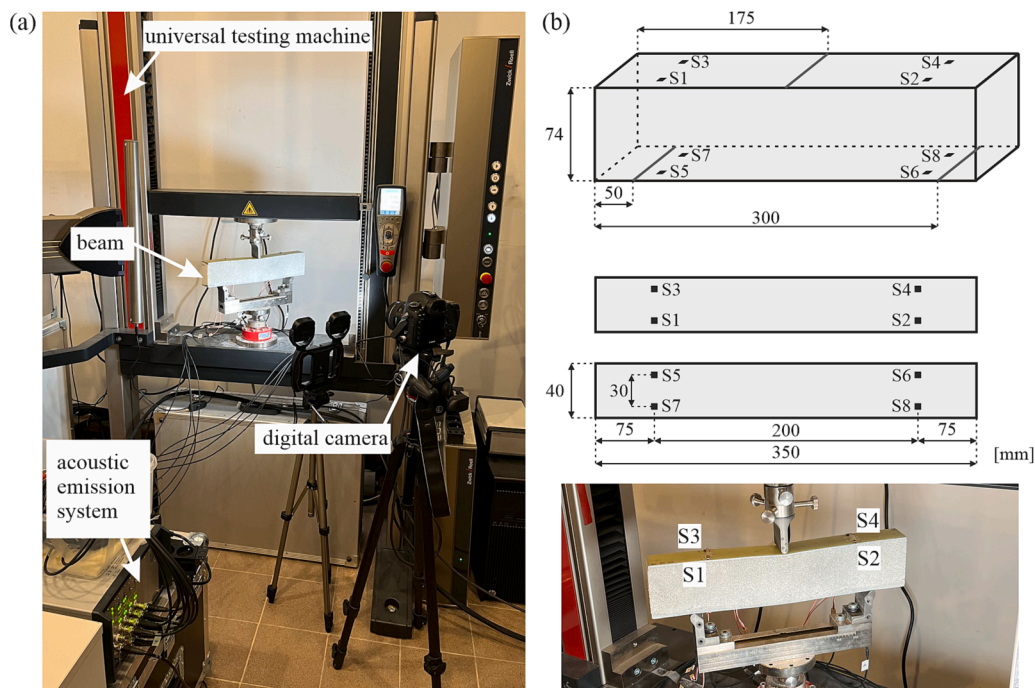

Fig. 3. Experimental setup: (a) equipment setting, (b) scheme of PZT sensors location.

the AMSY-6 system (Vallen Systeme GmbH) with a sampling rate of 10 MHz. A threshold of 30.1 dB was used to separate hits from background noise. AE signals were acquired in a frequency range of 40–500 kHz. The beam photographs were taken every 2 s with a Canon EOS 5D III digital camera. The images were then processed using ARAMIS Professional software (GOM GmbH, Braunschweig, Germany). The AE system was triggered with a testing machine, so the data was fully synchronised. The photographs were started manually at the moment of starting the bending process.

2.3. Digital image correlation

Digital image correlation (DIC) is a technique that is based on optical principles. It is used for full-field displacement and strain measurements of a loaded structure. The method is based on the matching of digital images between a non-deform state and subsequent deformed states. Changes in the coordinates of spots on random speckle patterns that cover the surface of the test object are calculated using the correlation coefficient [42]:

$$CC^{ZMN} = \frac{\sum_{i=1}^{M}\sum_{j=1}^{N}\left[\left(f(i,j) - u_f\right) \times \left(g(i,j) - u_g\right)\right]}{\sqrt{\sum_{i=1}^{M}\sum_{j=1}^{N}\left(f(i,j) - u_f\right)^2 \times \sum_{i=1}^{M}\sum_{j=1}^{N}\left(g(i,j) - u_g\right)^2}} \tag{1}$$

where f and g denote reference and target subsets, respectively, while u_f and u_g are intensities of reference and target subsets, respectively. The coefficient (1) is determined using the criterion of normalized zero-mean cross-correlation. In this study, the inspected region that covers the front surface of the sandwich beam was divided into subsets (facets) of a size of 19 × 19 pixels with a distance of 16 pixels. Then, the displacement and strain fields are calculated over the entire inspected area.

2.4. Acoustic emission

Acoustic emission (AE) measurements are based on the detection of elastic stress waves recorded by sensors. The micro- and macro-cracks emit elastic waves that propagate through the object. When such an elastic wave reaches a surface, it turns into a surface wave and causes its displacements. Sensors register the change and convert it into an electrical signal. Using the appropriate software, it is possible to observe the changes in real-time. Each micro- and macro-crack can be observed as a

short elastic wave signal.

The typical AE waveform is presented in Fig. 4. It gives the commonly used characteristics of the AE signals, including the duration, counts, amplitude and energy. In this study the fracture monitoring was investigated using typical AE parameters like cumulative energy, hits and cumulative hits.

3. Research results and discussion

3.1. Bending test results

The bending tests were performed with the constant cross-head displacement rate. Therefore, the displacement–time curves in all tests are the same and linear. The obtained load-time(displacement) curves of all performed tests are presented in Fig. 5. In each test result, four characteristic stages can be observed, they are: A - linear behaviour limit; B - first significant beam weakening; C - highest beam strength; D - failure or end of the test. All stages are marked in Fig. 5.

At first, the values of the linear behaviour limit were identified. Linear regression was performed based on the first bending phase for each beam. Comparing the results of the linear regression and the experimental data allowed to estimate the linear behaviour limit in particular beams. Then, the values for the other characteristic stages were read directly from the data graph. The gained values of force, cross-head displacement and respective time are listed in (Table 1).

The images of beams made of 'soft' foam (Beams #1-SD and #2-SI) during the test at characteristic moments are presented in Fig. 6. A clearly visible deflection of the beams under load and a significant deformation of the foam can be observed in the area where the force was applied.

Beam #1-SD behaved linearly until the force reached a value of 1.10 kN (stage A). The first significant beam weakening appeared after gaining 2.15 kN (stage B). Later, the force continued to increase, but much slower. After reaching the maximum force of 2.94 kN (stage C), there was a sharp drop in its value. Visual observation indicates that the reason for this was a sudden drop in the flexural stiffness of the upper laminate or a sudden increase in the core crush zone under the applied force. In Fig. 7 it can be noticed that the beam thickness decreased right below the punch and increased in its direct neighbourhood. The test was stopped after reaching the cross-head displacement of 30 mm (stage D). There was no abrupt failure that ended the beam bending. At the end of the test, very large crushing of the core and significant deformation of
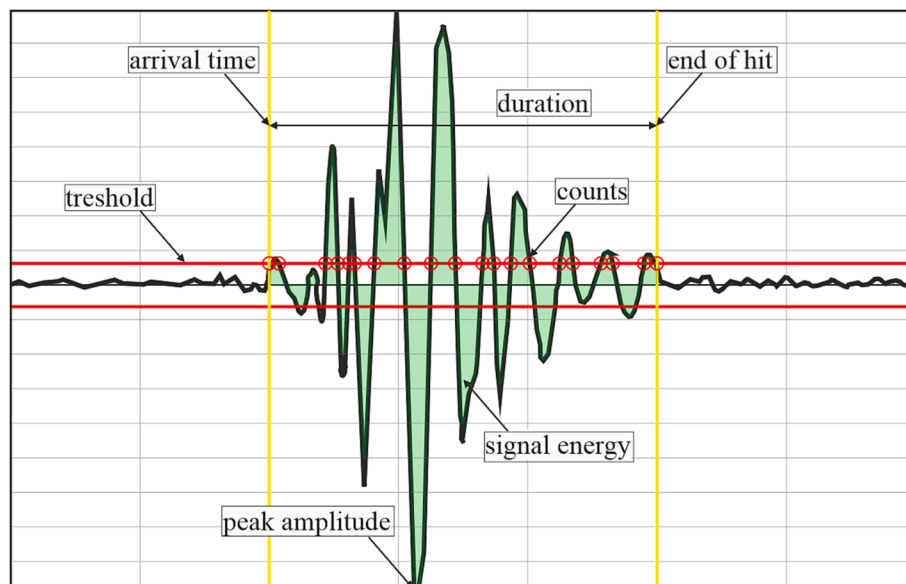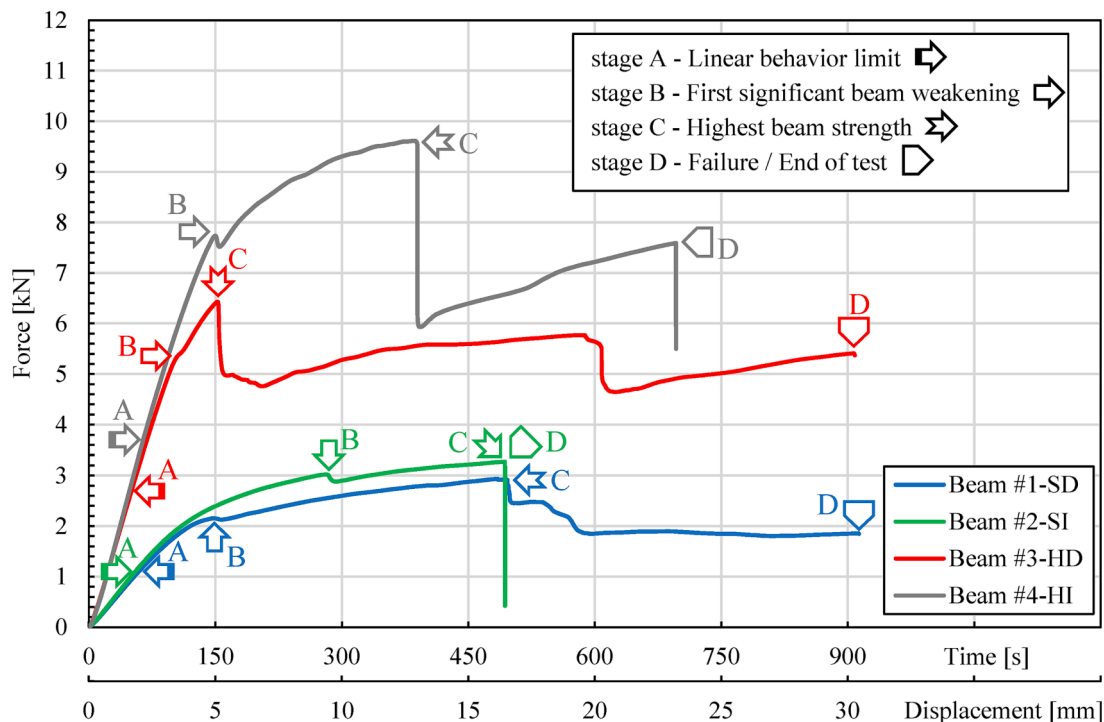

Fig. 4. Typical AE waveform.

Fig. 5. Load-time(displacement) curve for Beams #1÷#4.

Table 1

Characteristic values of force, cross-head displacement and respective time during bending – Beams #1÷#4.

Char. stage	force [kN]	displ. [mm]	time [s]	force [kN]	displ. [mm]	time [s]
	Beam #1-SD			Beam #2-SI		
A	1.10	1.94	60	1.10	1.82	56
B	2.15	4.89	148	3.02	9.35	282
C	2.94	16.13	486	3.27	16.42	494
D	1.85	30.38	914	3.27	16.42	494
	Beam #3-HD			Beam #4-HI		
A	2.70	1.66	52	3.70	2.12	64
B	5.21	3.31	100	7.74	4.96	150
C	6.43	5.05	152	9.61	12.82	386
D	5.37	30.22	908	7.59	23.18	696

the upper laminate were observed, there was an increase in displacement without an increase in force.

The Beam #2-SI bending process in the initial phase proceeded in a similar way as in Beam #1-SD. The identified linear behaviour limit of 1.10 kN (stage A) is the same. However, the first significant beam weakening (stage B) appeared much later, when the force reached the value of 3.02 kN. On the other hand, the maximum force of 3.27 kN (stage C) was achieved at about the same time as in Beam #1-SD, at the moment when the cross-head reached the displacement of about 16 mm. Right after reaching the maximum force, both Beams #1-SD and #2-SI experienced a sharp drop in force, in the case of Beam #2-SI it was the destructive moment (stage D). The core has been sheared throughout the entire width of the sample; see Fig. 6h and Fig. 8. The shear crack started under the top laminate, on the right side of the loading flat bar. Then, at an angle of about 45 degrees, it descended to the lower laminate. And finally, it caused a complete debonding of the core and the lower laminate. The test ended with a sudden beam failure.

The images of beams made of 'hard' foam (Beams #3-HD and #4-HI) during the test at characteristic moments are presented in Fig. 9. The flexural stiffness of the analysed beams was higher compared to the previous ones. Larger forces were recorded for analogous deflections.

Additionally, the deformation of the foam in the area where the force was applied was less extensive and more local.

The identified force of the linear behaviour limit (stage A) in Beam #3-HD is more than twice as high as in the previous beams and amounts to 2.70 kN. Furthermore, the behaviour of the beam was close to linear until the first weakening (stage B), which is 5.21 kN. Similarly to Beam #1-SD and #2-SI, after reaching the maximum force (stage C) of 6.43 kN, there was a sharp drop in its value. Visual observation indicates that the reason for this was a sudden delamination in the upper laminate that resulted in a local drop in its flexure stiffness on the right side of the punch; see Fig. 10a-b. Further, in the bending process, a second sharp drop in force was observed in about 600 s of the test duration. Fig. 10c-d shows how the damage propagated on the right side and how the new delamination occurred on the left side. There was no abruptly terminating the test failure during beam bending. The test was stopped after reaching the cross-head displacement of 30 mm (stage D). At the end of the test, very large crushing of the core and significant deformation of the upper laminate was observed, and the increase in force was very slow.

The process of bending Beam #4-HI in the initial phase proceeded in a similar way as in Beam #3-HD due to similar flexural stiffness. However, the force identified in the linear behaviour limit (stage A) has a much higher value of 3.70 kN. The same as in Beam #3-HD, the relationship between force and displacement was close to linear until the first weakening (stage B) of 7.74 kN. After this, the beam behaved nonlinearly up to the maximum force value (stage C) of 9.61 kN. Beam #4-HI had the highest load capacity of all the tests. After the maximum force was obtained, there was a sharp drop in its value. Visual observation indicates that the reason for this was the delamination of the laminate; see Fig. 11a-b. Despite the severe damage to the upper laminate, the beam still retained its partial load-bearing capacity until the core was sheared off, causing the final sudden failure (stage D); see Fig. 11c-d.

3.2. Digital image correlation results

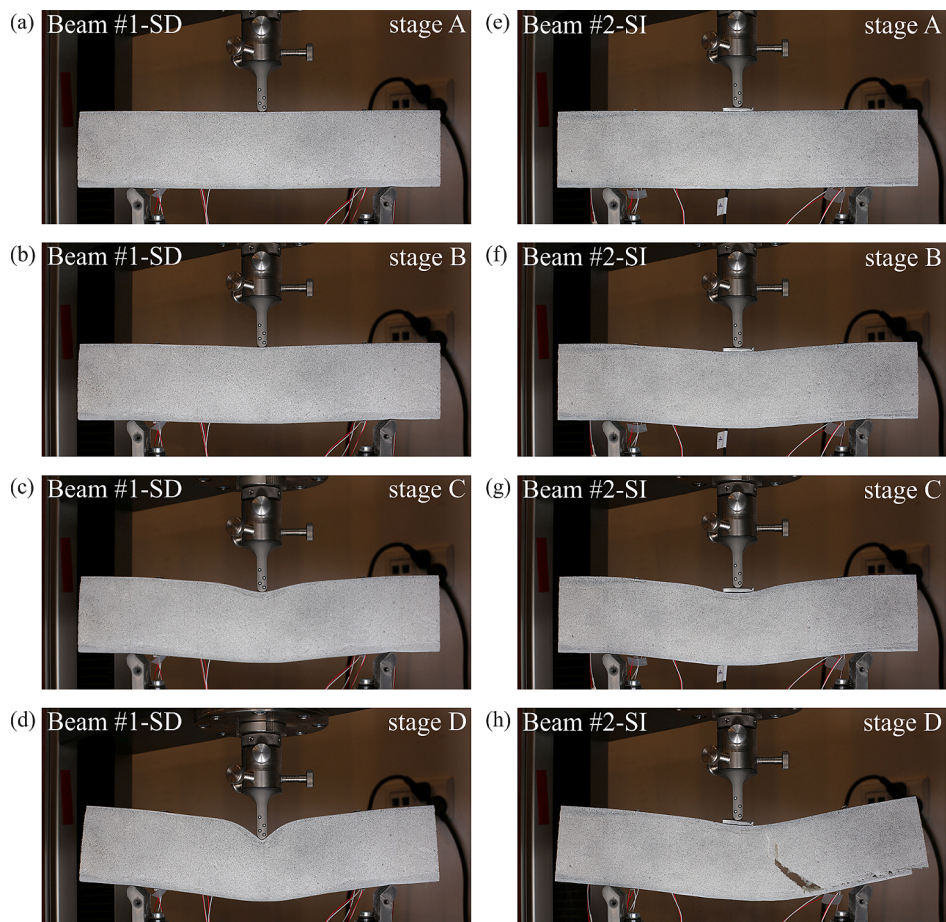The selected results of the DIC analysis on the side surface of

Fig. 6. Deformations of beams in selected stages during bending: (a)÷(d) Beam #1-SD, (e)÷(h) Beam #2-SI.
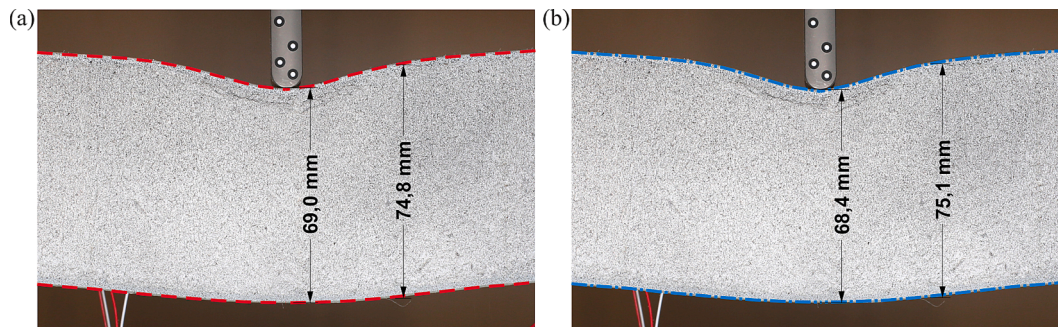

Fig. 7. Beam #1-SD during bending: (a) at the characteristic stage C of the highest beam strength (486 s), (b) right after stage C (488 s).
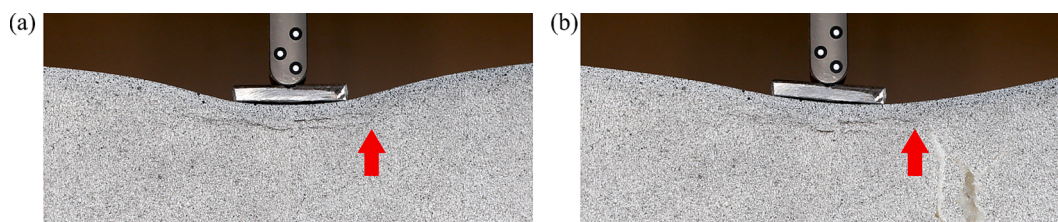

Fig. 8. Zooming in on the force point in Beam #2-SI during bending: (a) just before failure – stage D (494 sec.), (b) after failure (496 sec.).

sandwich beams made 'soft' foam (Beams #1-SD and #2-SI) during the bending process are presented in Fig. 12. In this study, to observe the fracture process of the sandwich beams, equivalent Mises strain distribution was examined.

The first results Fig. 12a and Fig. 12e, for Beams #1-SD and #2-SI, respectively, show the field strain distribution in an early stage of
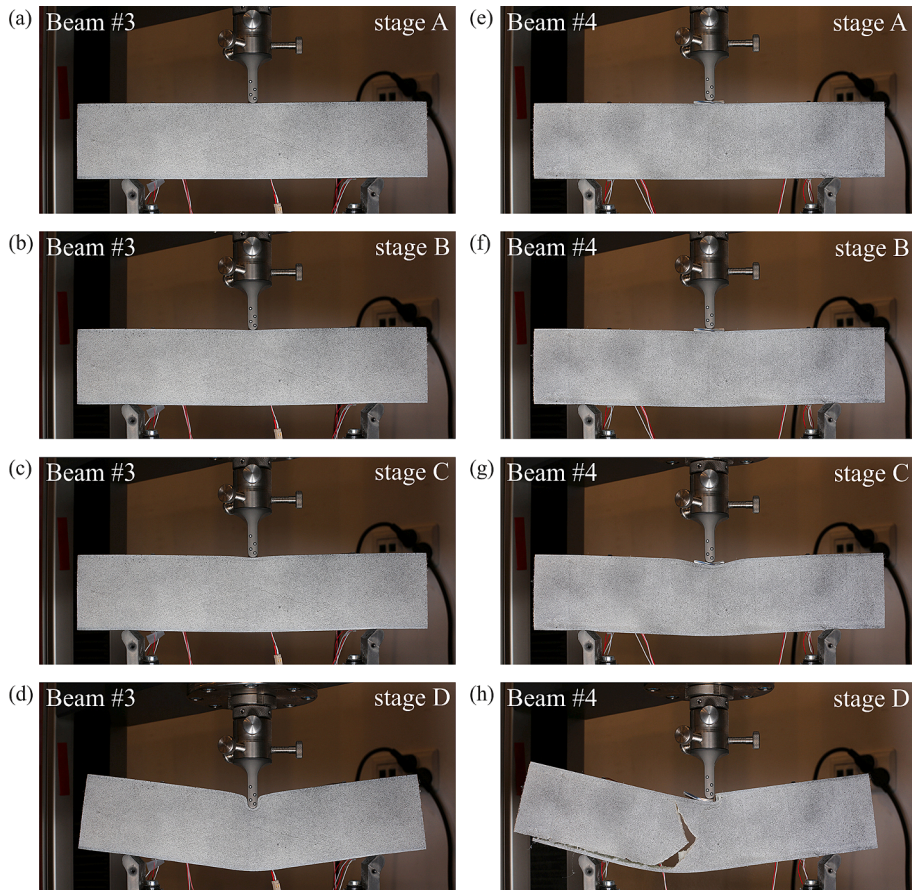
Fig. 9. Deformations of beams in selected stages during bending: (a)÷(d) Beam #3-HD, (e)÷(h) Beam #4-HI.
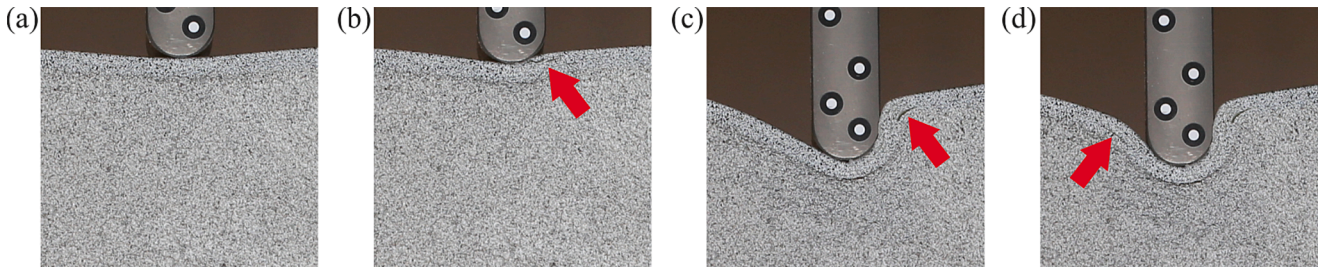

Fig. 10. Zooming in on the force point in Beam #3-HD during bending: (a) highest beam strength – stage C (152 s), (b) damage after the first sharp drop in force (160 s), (c) damage before the second sharp drop in force (590 s), (d) damage after the second sharp drop in force (620 s).
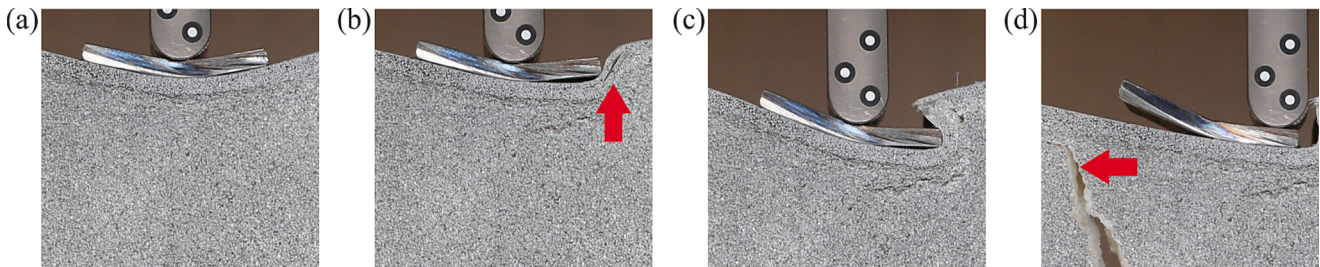

Fig. 11. Zooming in on the force point in Beam #4-HI during bending: (a) highest beam strength – stage C (386 s), (b) damage after a sharp drop in force (388 s), (c) damage before final failure – stage D (696 s), (d) final failure (698 s).

bending. It is the characteristic stage A, when the limit of the linear force–displacement relation has been reached. The first observation is that the core strains in both beams were still within the conventional elastic zone limit, i.e. less than 1.8%. The characteristic is that the distinct zones with low strain values in areas outside the support points are clearly visible (marked with red borders). This is due to the low shear
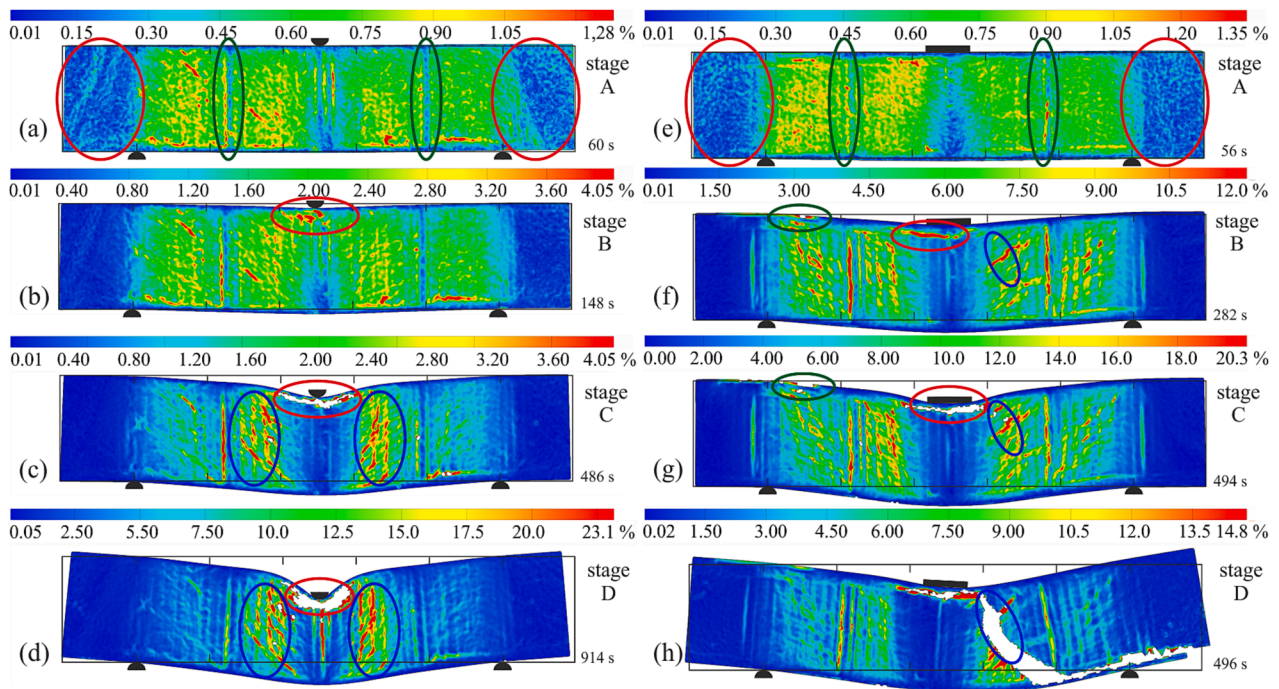
Fig. 12. DIC analysis results: (a)-(d) Beam #1-SD, (e)-(h) Beam #2-SI.

modulus of the core. Fig. 13 shows an example of Beam #1-SD during bending, where clear cut-off lines of the core shear deformation over the support points are visible. The next noticeable effect is the locations of the welded surfaces in the core (marked with green borders). They form a kind of rib in the foam structure. The described effects are magnified as the beam deflection increased, which can be observed in further figures.

The results for characteristic stage B, the first significant beam weakening, are presented in Fig. 12b and Fig. 12f. In the area where the force was applied (marked with a red border), the core strains signifi-cantly exceeded the value of the conventional elastic zone in both beams (1.8%). Furthermore, in Beam #1-SD those strains were close to the strain value corresponding to compressive strength (5.9%), while in Beam #2-SI they were well above this value. The application of the distributed force caused Beam #2-SI to weaken much later than Beam #1-SD. From stage B, the core under applied force was continuously crushed (red border), resulting in a much slower growth rate of the force. What is characteristic at this stage of the bending process in Beam #2-SI (Fig. 12f), is a high intensity of shear strains, which can be observed to the right of the applied force (marked with a blue border) and a concentration of strains close to the upper laminate, above the left support (marked with green border). A closer analysis of the photos showed that at the point above the left support, debonding of the core and the laminate occurred. It expanded with the bending process; see Fig. 14.

The results for characteristic stage C, the highest beam strength moment, are presented in Fig. 12c and Fig. 12g. It can be seen that the

core was already significantly crushed under force (red border), and some of the points observed by the DIC system become invisible. There was also a significant shear effect on the core on both sides of the applied force (blue borders). In Beam #2-SI previously mentioned strain con-centration on the right side of the force increased significantly (blue border).

At the end of the test (stage D) all of the above effects have been intensified (Fig. 12d and Fig. 12h). In Beam #1-SD there was no sudden failure, while in Beam #2-SI the core was sheared exactly in the area which already had been marked with a blue border in Fig. 12f-g.

The selected results of the DIC analysis on the side surface of the beams made of 'hard' foam (Beams #3-HD and #4-HI) are presented in Fig. 15.

The sequence of results presented is the same as for the 'soft' foam beams. Initially, the field strain distributions in an early stage of bending (stage A) are presented in Fig. 15a and Fig. 15f, for Beams #3-HD and #4-HI, respectively. Similarly to previous results, strains in the core areas outside the support points almost do not increase (marked with red borders). The difference from the previous results is that the strains were much more clearly concentrated around the support points and the applied force from the early beginning of the bending process. The location of the welded surfaces in the core structure can be noticed, but in the 'hard' foam it is much less visible (marked with green borders). The moment of the first significant beam weakening (stage B) occurred when the strains in the core under force reached their value of the conventional elastic zone (2.0%) in Beam #3-HD (Fig. 15b) and was
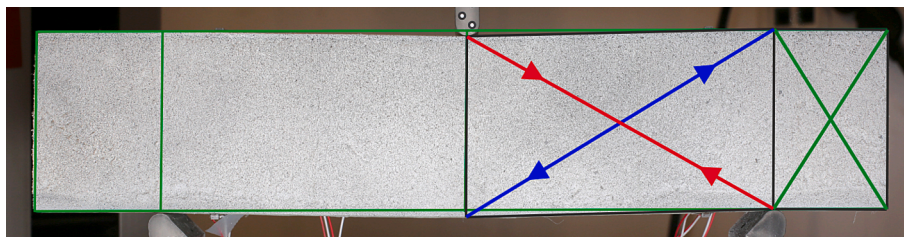

Fig. 13. Deformation of Beam #1-SD after exceeding the limit of linear behaviour (90 s).
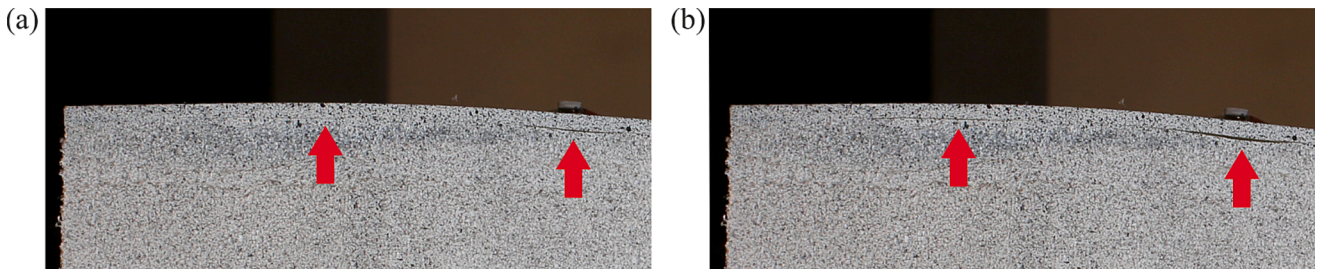
Fig. 14. Zooming in on the debonding area in Beam #2-SI during bending: (a) stage B - first significant beam weakening (282 s), (b) stage C - highest beam strength (494 s).
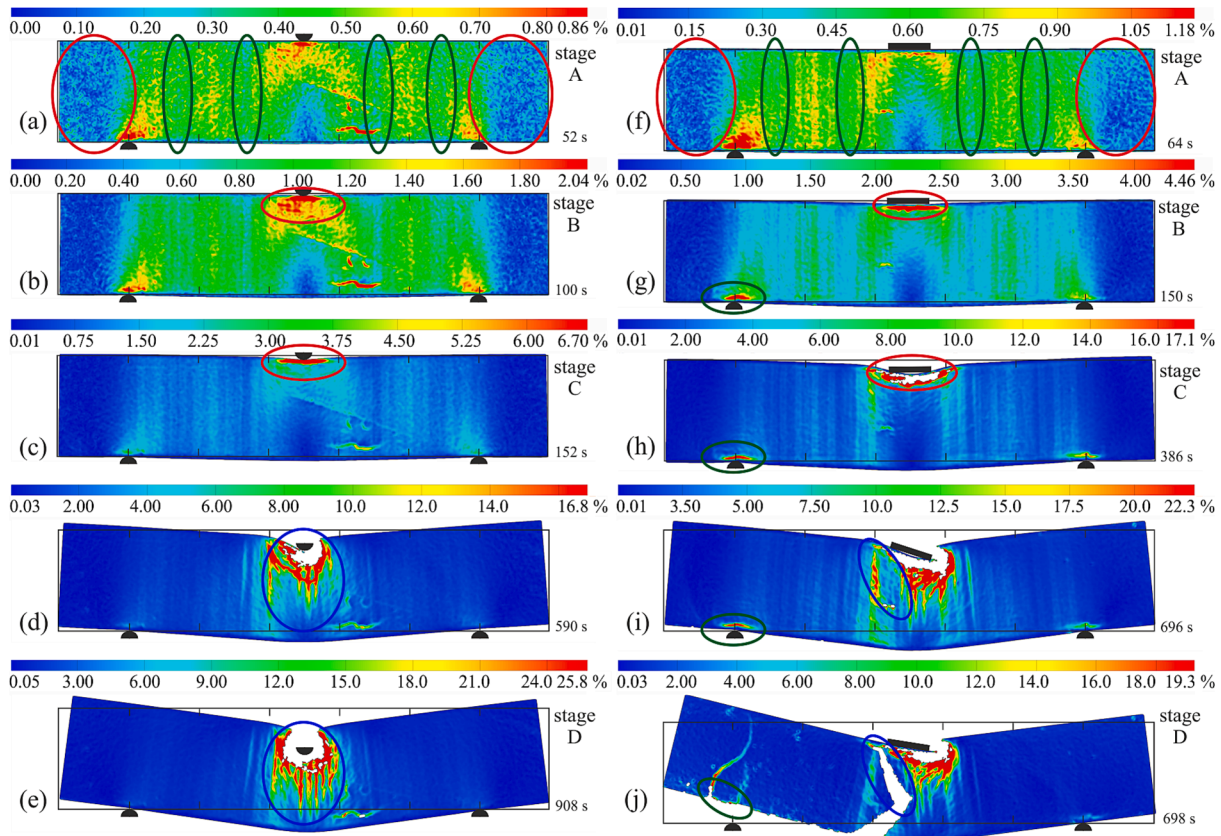

Fig. 15. DIC analysis results: (a)-(e) Beam #3-HD, (f)-(j) Beam #4-HI.

close to the value of the strain corresponding to the compressive strength (5.3%) in Beam #4-HI (Fig. 15g). The application of the distributed force caused Beam #4-HI to weaken later, but this interval is not as long as in beams made of 'soft' foam. What is characteristic at this stage of the bending process in Beam #4-HI is a very asymmetric concentration of strains over the supports. The strain values above the left support were much higher (green border in Fig. 15g). They were growing with the

bending process and at the same time becoming more and more concentrated; see Fig. 15h-i. Finally, the core fractured at this point during the final failure; see Fig. 15j. This effect was not visible before its final destruction; see Fig. 16.

When the maximum force was reached (stage C), the concentration of strains around the applied force became even more apparent (red border in Fig. 15c and Fig. 15h). Their values exceeded the strain
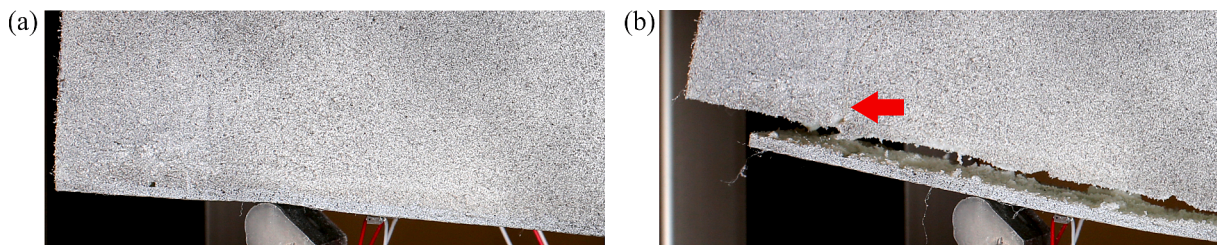

Fig. 16. Zooming in on the left support area in Beam #4-HI during bending: (a) before final failure – stage D (696 s), (b) after final failure (698 s).

corresponding to the compressive strength in both beams. The very local plasticization of the foam around the applied force made the bedding for the upper laminate very unstable and, as a consequence, it was broken in both beams, see Fig. 10b and Fig. 11b.

Beam #3-HD before the end of the bending process experienced a second sudden drop in strength in 590 s of the test (Fig. 10c). The result for that moment is presented in Fig. 15d.

At the end of the test (stage D), a large crushing of the core occurred directly under the force (Fig. 15e and Fig. 15j). In Beam #4-HI, the strain distribution just before the final failure makes it possible to recognize the location of a further fracture (blue border in Fig. 15i). It actually occurred at the indicated place, leading to the final failure (blue border in Fig. 15j).

3.3. Acoustic emission results

The first results presented are the cumulative energy charts for particular groups of sensors (results from doubled sensors are added): S1 + S3 (top left), S2 + S4 (top right), S5 + S7 (bottom left), S6 + S8 (bottom right), these are shown in Fig. 17. Additionally, the load-time curve have been added to the presented results for a clearer view of the bending process stages. The characteristic stages identified earlier are marked on the graph by letters and background colours.

The analysis of the results obtained shows similarities. During the initial 0-A phase, there is no evident change in energy in any of the beams. The first energy growths appear in the A-B interval when the linear phase is already exceeded. It is noticeable that the growth in energy is more intense in the results recorded by the sensors located in the lower laminates. A possible reason is that these sensors are in the immediate vicinity of the supports, closer to the point action of the re-action forces. In the B-C phase, after the first significant beam weakening, single energy spikes were recorded. They are mainly observed in the upper laminate sensors, indicating that the applied force evoked an early stage of damage to the laminate or a foam crushing near the punch. Single energy spikes occurred at moments that corresponded to changes in the rate of the force–time curve. At stage C which is assigned to the highest beam strength in all beams except Beam #2-SI, a sharp jump in the energy of the upper laminate sensors may be observed on both sides of the specimens, or on only one side if the damage is very unsymmetrical, such as in Beam #4-HI (see Fig. 11b). This is due to the delamination/breakage of the laminate structure and, therefore, the clear penetration of the punch into the beam structures. Beam #2-SI lacks such an effect because stage C is also associated with the final failure. Its destructive moment, caused by the shear of the core, was recorded most intensively by the S6 + S8 sensors located on the right side of the bottom surface of the composite beam, which corresponds to the location of the core crack. The subsequent C-D phase shows smaller energy peaks associated with continuously increasing damage to the upper laminate surface. The final failure of Beam #4-HI was recorded the most intensively by sensors S5 + S7, where the highest energy spike may be observed. These sensors also correspond to the location of the core crack.

The appearing hits recorded per second are the next data collected during the tests that have been considered. The compilation of the following graphs: appearing hits in all sensors (scatter plot), cumulative hits for groups of sensors, and load-time curves are presented in Fig. 18. The characteristic stages are also marked on this graph in the same way as in previous cumulative energy plots.
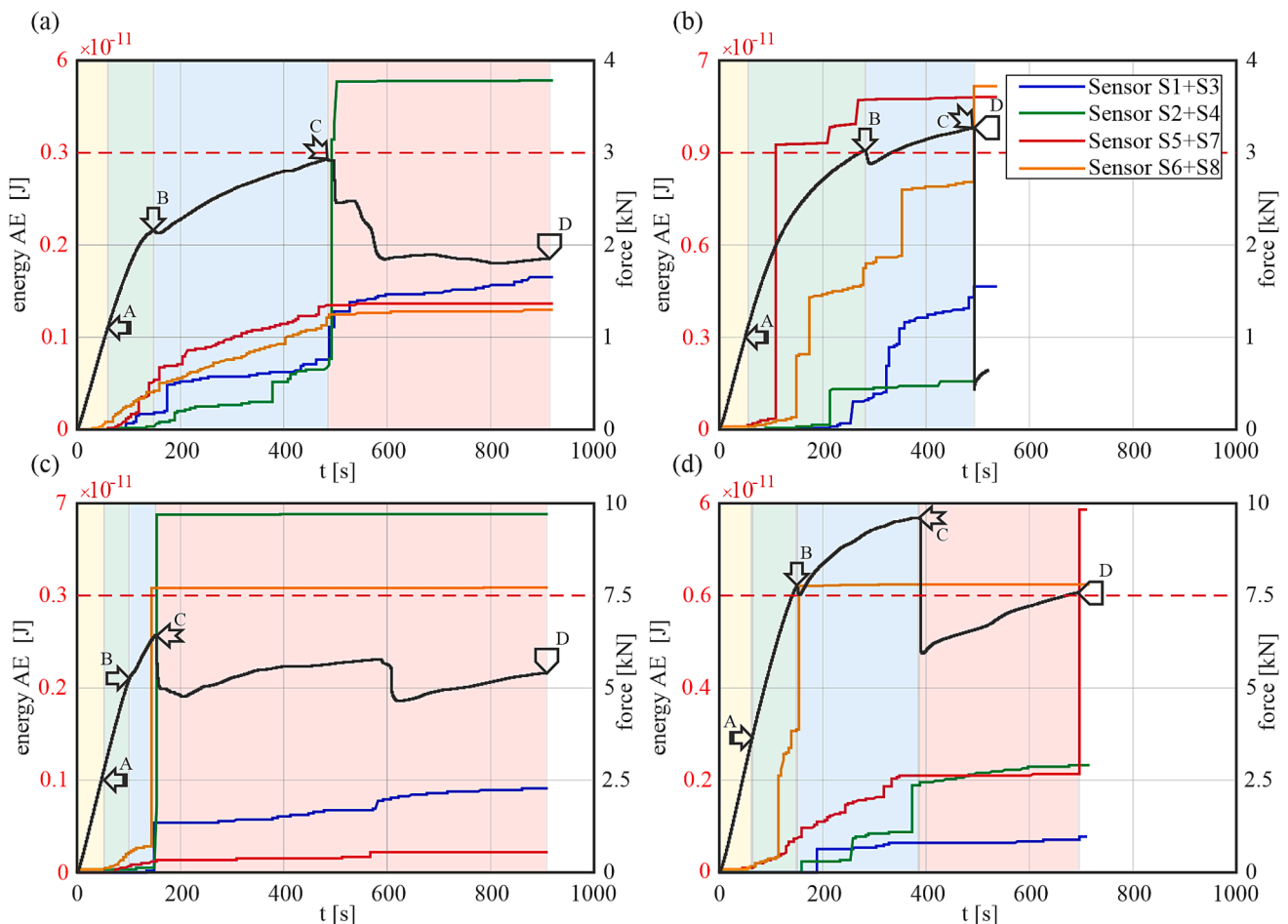

Fig. 17. AE analysis results – cumulative energy for particular groups of sensors: a) Beam #1-SD, b) Beam #2-SI, c) Beam #3-HD, d) Beam #4-HI.
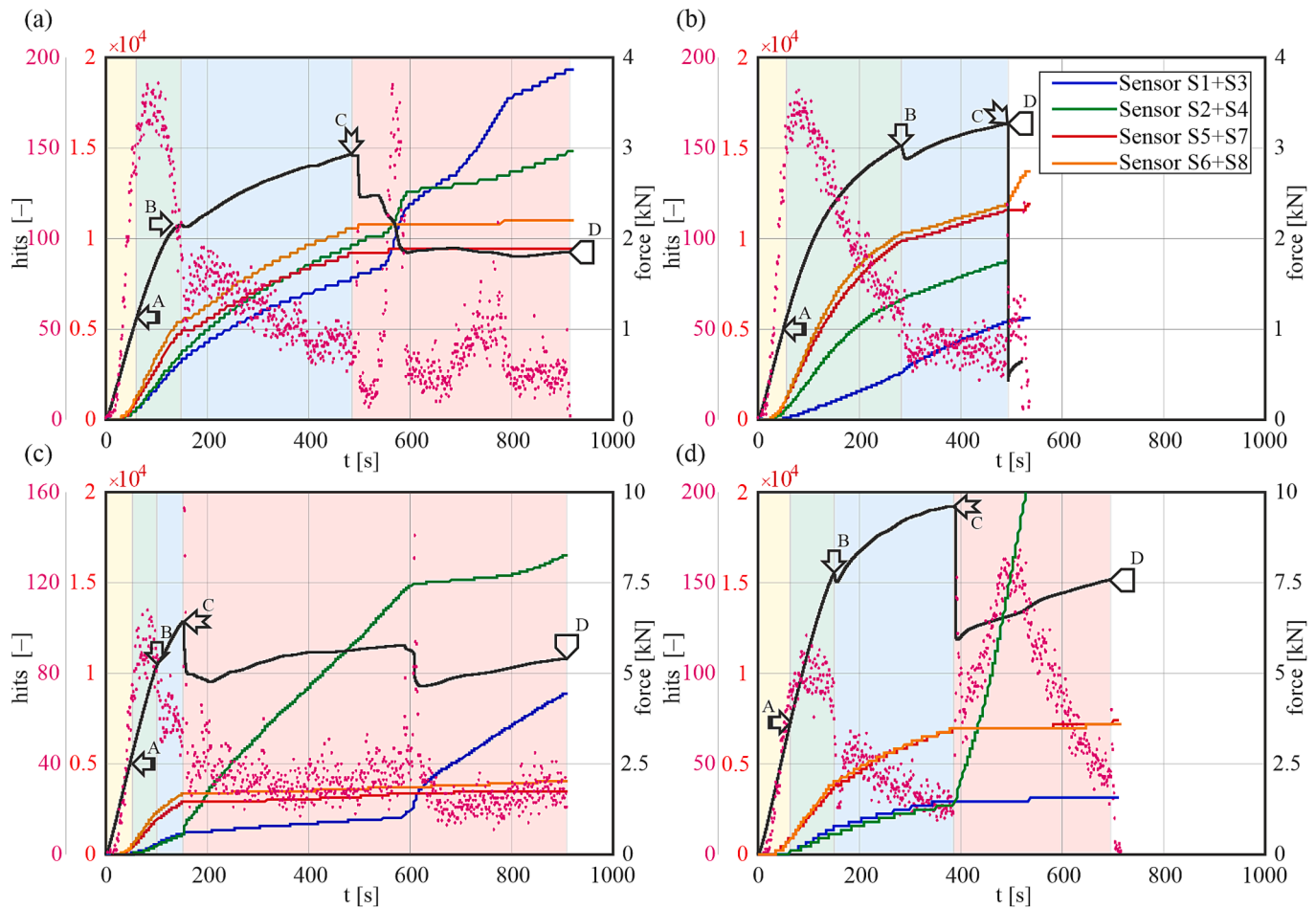
Fig. 18. AE analysis results – cumulative hits for particular groups of sensors: a) Beam #1-SD, b) Beam #2-SI, c) Beam #3-HD, d) Beam #4-HI.

When comparing the graphs for all tested beams, some consistencies can be noticed. In the initial phase of loading 0-A, there is a rapid increase in registered hits per second. What is characteristic, this phenomenon is not accompanied by a rapid growth of cumulative hits nor cumulative energy (see Fig. 17). It can be concluded that during the linear behaviour of the beam, the total number of hits is not large, but they occur in abrupt short in time series characterized by very low energy. The rapid increase in hits ends just after stage A is passed. During the A-B interval, there is a stabilization in the number of hits per second, and then a decrease. At the same time, there is a rapid growth of cumulative hits. This means that the total number of hits increases much faster, but it happens less rapidly, that is, more evenly distributed over time. At this stage, it is noticeable that the lower laminate sensors register more hits than the upper ones. After the first significant beam weakening (stage B) in all beams, the number of hits registered per second stabilizes. The cumulative hits parameter still increases but is noticeably slower than in the previous phase. In all beams, except Beam #2-SI there is no significant difference in the rate of its growth on the left and right sides of the beam. In Beam #2-SI, the upper right sensors S2 + S4 register much more hits than the upper left ones S1 + S3. The most likely cause of such a phenomenon is damage propagation in the vicinity of those (upper right) sensors; see the DIC results in Fig. 12f-g. Finally, the core was sheared on the side where more hits were recorded.

After the highest beam strength (stage C), the situation changes depending on the beam. Beam #2-SI is already broken. In Beam #1-SD the number of hits registered by the left and right upper sensors increased significantly. This means that the main damage process occurred in the upper laminate, which is confirmed by the observations (Fig. 7) and the DIC results (Fig. 12c-d). In Beam #3-HD after the first

sharp drop in force, there was an increase in the registered number of hits mainly in the upper right sensors S2 + S4, in turn after the second sharp drop in force the situation reversed and the main increase moved to the upper left sensors S1 + S3. This phenomenon fits perfectly with the observation of how the damage propagated in the upper laminate shown in Fig. 10. In Beam #4-HI after stage C the main increase in registered hits may be observed only in the upper right sensors S2 + S4. It fits perfectly with the observation shown in Fig. 11.

The above analysis showed that in the considered task a better picture of the beams behaviour was obtained by examining the cumulative hits rather than the cumulative energy. These results allowed for better identification and localization of damage that occurred during the bending process. It turns out that even such a rough result as shown in Fig. 19, which is the total number of hits for particular groups of sensors, gives the possibility to draw conclusions. In Beam #1-SD there is almost an equal number of hits registered by the upper sensors S1 + S3 and S2 + S4 and their number is much higher than in the lower sensors. This means that the damage process was close to symmetric and took place mainly in the upper laminate. In Beam #3-HD the situation is similar to Beam #1-SD but it is clearly seen that the damage process was more dominant on the right side where the main delamination in the upper laminate occurred. In Beam #2-SI most events are recorded by lower sensors, while dominant are right sensors S6 + S8 where the final core-laminate debonding occurred. In Beam #4-HI the sensors that recorded the highest number of hits are in the upper right S2 + S4. This is the side where the main delamination and breakage of the laminate occurred. All these conclusions are consistent with the previous observations.
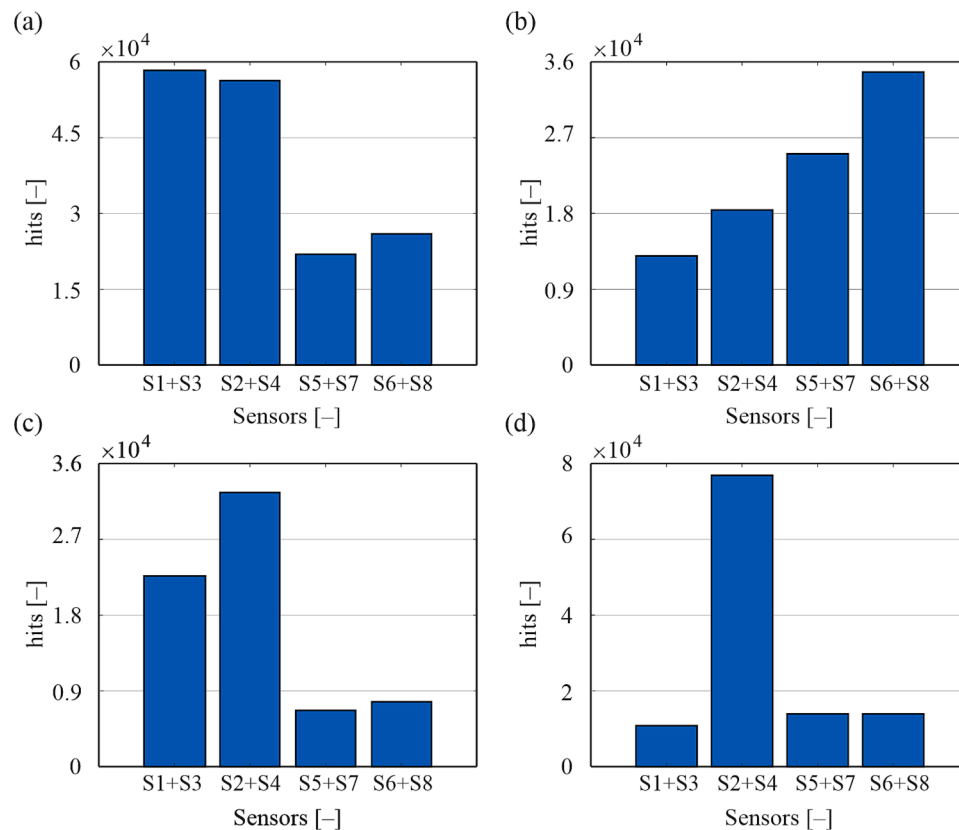
Fig. 19. AE analysis results – number of hits for particular groups of sensors: a) Beam #1-SD, b) Beam #2-SI, c) Beam #3-HD, d) Beam #4-HI.

4. Conclusions

This paper dealt with the failure process characterisation of sandwich beams, carried out by the application of two integrated non-destructive methods. Acoustic and optical testing was used for this purpose. From the results obtained, the following conclusions could be formulated.

- The research program performed allowed observing various modes of failure in composite beams.
- Two integrated non-destructive testing techniques: acoustic emission and digital image correlation allowed more detailed observations of the bending process under concentrated force and distributed load. DIC made possible observation of the full-field surface distribution of the strains in a sandwich beam core. It allowed for accurate tracking of the fracture process, moreover, it highlighted welded surfaces in the core. Observation of the development of the strain concentration progressing with increasing load allows highlighting the weakening points, and consequently earlier localisation of the failure areas, i.e. plasticised zones or cracks in the foam. AE allowed registering signals concerning damage evolution from the entire volume of the beam. The obtained results, i.e. energy and hits charts, allowed for detailing the various stages of beam work and failure. AE also made it possible to locate damage that occurred by the number of events recorded by the sensors. The closer the sensor was to the damage, the more events with higher energy it registered.
- The classification of damage stages was proposed by indicating characteristic stages of the behaviour of the sandwich beams. These stages were clearly recognisable in the AE results when analysing the cumulative hits for particular groups of sensors, as well as when observing the strain fields from the DIC, in particular the plasticization zones of the foam.

- The application of two integrated methods enhanced the failure characterisation process, especially in the context of quantitative damage assessment. The DIC technique provided quantitative measurement until a structure is consistent. When a crack occurred, only qualitative measurement remained in a damaged area as using the DIC method it was not possible to obtain precise values of strains within the cracks because there was no material left. After cracking a structure, AE continued both quantitative and qualitative measurements providing the values of the number of hits and the energy of AE events.

In summary, the presented research showcases the benefits of integrated DIC and AE techniques and why they should be considered as reliable techniques for composite sandwich structure failure analysis. Further work will focus on determining the location of the failure more precisely by proposing an original method of the collected acoustic signals analysis.

CRediT authorship contribution statement

Łukasz Pyrzowski: Conceptualization, Methodology, Investigation, Formal analysis, Visualization, Writing – original draft. **Magdalena Knak:** Conceptualization, Methodology, Investigation, Formal analysis, Visualization, Writing – original draft. **Magdalena Rucka:** Conceptualization, Methodology, Investigation, Formal analysis, Writing – review & editing, Supervision, Project administration, Funding acquisition.

Declaration of Competing Interest

The authors declare that they have no known competing financial interests or personal relationships that could have appeared to influence the work reported in this paper.

References

[1] Davalos JF, Chen A, Zou B. Performance of a scaled FRP deck-on-steel girder bridge model with partial degree of composite action. Eng Struct 2012;40:51–63. https://doi.org/10.1016/j.engstruct.2012.02.020.

[2] Siwowski T, Kaleta D, Rajchel M. Structural behaviour of an all-composite road bridge. Compos Struct 2018;192:555–67. https://doi.org/10.1016/j.compstruct.2018.03.042.

[3] Uyttersprot J, De Corte W. Measured dynamic properties of web-core sandwich panel FRP composite footbridges and their relation to pedestrian comfort analysis. Compos Struct 2021;259:113236. https://doi.org/10.1016/j.compstruct.2020.113236.

[4] Young S, Penumadu D, Patchen AD, Laggis G, Michaud J, Bradley A, et al. Smart Polymer Composite Deck Monitoring Using Distributed High Definition and Bragg Grating Fiber Optic Sensing. Sensors 2022:22. https://doi.org/10.3390/s22114089.

[5] Dos SFM, Mohan M. Train buffeting measurements on a Fibre-reinforced plastic composite footbridge. Struct Eng Int J Int Assoc Bridg Struct Eng 2011;21:285–9. https://doi.org/10.2749/101686611X13049248220087.

[6] Chróścielewski J, Miśkiewicz M, Pyrzowski Ł, Sobczyk B, Wilde K. A novel sandwich footbridge - Practical application of laminated composites in bridge design and in situ measurements of static response. Compos Part B Eng 2017;126: 153–61. https://doi.org/10.1016/j.compositesb.2017.06.009.

[7] Mousa MA, Uddin N. Flexural Behavior of Full-Scale Composite Structural Insulated Floor Panels. Adv Compos Mater 2011;20:547–67. https://doi.org/10.1163/156855111X610208.

[8] Keller T, Haas C, Vallée T. Structural Concept, Design, and Experimental Verification of a Glass Fiber-Reinforced Polymer Sandwich Roof Structure. J Compos Constr 2008;12:454–68. https://doi.org/10.1061/(ASCE)1090-0268(2008)12:4(454).

[9] Smakosz Ł, Kreja I, Pozorski Z. Flexural behavior of composite structural insulated panels with magnesium oxide board facings. Arch Civ Mech Eng 2020;20:105. https://doi.org/10.1007/s43452-020-00109-y.

[10] Fam A, Sharaf T. Flexural performance of sandwich panels comprising polyurethane core and GFRP skins and ribs of various configurations. Compos Struct 2010;92:2927–35. https://doi.org/10.1016/j.compstruct.2010.05.004.

[11] Islam MM, Aravinthan T. Behaviour of structural fibre composite sandwich panels under point load and uniformly distributed load. Compos Struct 2010;93:206–15. https://doi.org/10.1016/j.compstruct.2010.05.019.

[12] Kulpa M, Siwowski T. Stiffness and strength evaluation of a novel FRP sandwich panel for bridge redecking. Compos Part B Eng 2019;167:207–20. https://doi.org/10.1016/j.compositesb.2018.12.004.

[13] Bahabadi HM, Farrokhabadi A, Rahimi GH. Investigation of debonding growth between composite skins and corrugated foam-composite core in sandwich panels under bending loading. Eng Fract Mech 2020;230:106987. https://doi.org/10.1016/j.engfracmech.2020.106987.

[14] Mei J, Liu J, Huang W. Three-point bending behaviors of the foam-filled CFRP X-core sandwich panel: Experimental investigation and analytical modelling. Compos Struct 2022;284:115206. https://doi.org/10.1016/j.compstruct.2022.115206.

[15] Xie H, Shen C, Fang H, Han J, Cai W. Flexural property evaluation of web reinforced GFRP-PET foam sandwich panel: Experimental study and numerical simulation. Compos Part B Eng 2022;234:109725. https://doi.org/10.1016/j.compositesb.2022.109725.

[16] Wang L, Liu W, Wan L, Fang H, Hui D. Mechanical performance of foam-filled lattice composite panels in four-point bending: Experimental investigation and analytical modeling. Compos Part B Eng 2014;67:270–9. https://doi.org/10.1016/j.compositesb.2014.07.003.

[17] Mathieson H, Fam A. Numerical modeling and experimental validation of axially loaded slender sandwich panels with soft core and various rib configurations. Eng Struct 2016;118:195–209. https://doi.org/10.1016/j.engstruct.2016.03.044.

[18] Taghipoor H, Eyvazian A, Musharavati F, Sebaey TA, Ghiaskar A. Experimental investigation of the three-point bending properties of sandwich beams with polyurethane foam-filled lattice cores. Structures 2020;28:424–32. https://doi.org/10.1016/j.istruc.2020.08.082.

[19] Liu J, Tao J, Li F, Zhao Z. Flexural properties of a novel foam core sandwich structure reinforced by stiffeners. Constr Build Mater 2020;235:117475. https://doi.org/10.1016/j.conbuildmat.2019.117475.

[20] Liu Z, Liu J, Zhang M, Liu J, Huang W. Study of three-point bending behaviors of composite sandwich structure with re-entrant honeycomb cores. Polym Compos 2022. https://doi.org/10.1002/pc.27128.

[21] Balıkoğlu F, Demircioğlu TK. Flexural behaviour of the composite sandwich beams with grid-scored foam: Experimental and theoretical approach. Thin-Walled Struct 2022;171:108691. https://doi.org/10.1016/j.tws.2021.108691.

[22] Jerabek M, Major Z, Lang RW. Strain determination of polymeric materials using digital image correlation. Polym Test 2010;29:407–16. https://doi.org/10.1016/j.polymertesting.2010.01.005.

[23] Fathi A, Keller J-H, Altstaedt V. Full-field shear analyses of sandwich core materials using Digital Image Correlation (DIC). Compos Part B Eng 2015;70:156–66. https://doi.org/10.1016/j.compositesb.2014.10.045.

[24] Ramakrishnan KR, Guérard S, Maheo L, Shankar K, Viot P. A new method for the study of parabolic impact of foam-core sandwich panels. Compos Part B Eng 2019; 167:717–27. https://doi.org/10.1016/j.compositesb.2019.02.062.

[25] Sayahlatifi S, Rahimi GH, Bokaei A. The quasi-static behavior of hybrid corrugated composite/balsa core sandwich structures in four-point bending: Experimental study and numerical simulation. Eng Struct 2020;210:110361. https://doi.org/10.1016/j.engstruct.2020.110361.

[26] Masmoudi S, El Mahi A, El Guerjouma R. Mechanical behaviour and health monitoring by acoustic emission of sandwich composite integrated by piezoelectric implant. Compos Part B Eng 2014;67:76–83. https://doi.org/10.1016/j.compositesb.2014.05.032.

[27] Koziol M, Figlus T. Failure progress of 3D reinforced GFRP laminate during static bending, evaluated by means of acoustic emission and vibrations analysis. Materials (Basel) 2015;8:8751–67. https://doi.org/10.3390/ma8125490.

[28] Maillet E, Baker C, Morscher GN, Pujar VV, Lemanski JR. Feasibility and limitations of damage identification in composite materials using acoustic emission. Compos Part A Appl Sci Manuf 2015;75:77–83. https://doi.org/10.1016/j.compositesa.2015.05.003.

[29] Kahirdeh A, Khonsari MM. Acoustic entropy of the materials in the course of degradation. Entropy 2016:18. https://doi.org/10.3390/e18080280.

[30] Saeedifar M, Fotouhi M, Ahmadi Najafabadi M, Hosseini Toudeshky H, Minak G. Prediction of quasi-static delamination onset and growth in laminated composites by acoustic emission. Compos Part B Eng 2016;85:113–22. https://doi.org/10.1016/j.compositesb.2015.09.037.

[31] Mohammadi R, Najafabadi MA, Saeedifar M, Yousefi J, Minak G. Correlation of acoustic emission with finite element predicted damages in open-hole tensile laminated composites. Compos Part B Eng 2017;108:427–35. https://doi.org/10.1016/j.compositesb.2016.09.101.

[32] Chandarana N, Sanchez DM, Soutis C, Gresil M. Early damage detection in composites during fabrication and mechanical testing. Materials (Basel) 2017:10. https://doi.org/10.3390/ma10070685.

[33] Brunner AJ. Identification of damage mechanisms in fiber-reinforced polymer-matrix composites with Acoustic Emission and the challenge of assessing structural integrity and service-life. Constr Build Mater 2018;173:629–37. https://doi.org/10.1016/j.conbuildmat.2018.04.084.

[34] Rescalvo FJ, Valverde-Palacios I, Suarez E, Roldán A, Gallego A. Monitoring of carbon fiber-reinforced old timber beams via strain and multiresonant acoustic emission sensors. Sensors (Switzerland) 2018:18. https://doi.org/10.3390/s18041224.

[35] Esola S, Wisner BJ, Vanniamparambil PA, Geriguis J, Kontsos A. Part qualification methodology for composite aircraft components using acoustic emission monitoring. Appl Sci 2018:8. https://doi.org/10.3390/app8091490.

[36] Pashmforoush F, Khamedi R, Fotouhi M, Hajikhani M, Ahmadi M. Damage Classification of Sandwich Composites Using Acoustic Emission Technique and k-means Genetic Algorithm. J Nondestruct Eval 2014;33:481–92. https://doi.org/10.1007/s10921-014-0243-y.

[37] Sikdar S, Mirgal P, Banerjee S, Ostachowicz W. Damage-induced acoustic emission source monitoring in a honeycomb sandwich composite structure. Compos Part B Eng 2019;158:179–88. https://doi.org/10.1016/j.compositesb.2018.09.071.

[38] Abdulaziz AH, Hedaya M, Elsabbagh A, Holford K, McCrory J. Acoustic emission wave propagation in honeycomb sandwich panel structures. Compos Struct 2021; 277:114580. https://doi.org/10.1016/j.compstruct.2021.114580.

[39] Rishikesan V, Chaturvedi B, Arunachalam N. Characterisation of drilling-induced damage in GFRP Honeycomb Sandwich Composites using Acoustic Emission. Procedia Manuf 2021;53:664–72. https://doi.org/10.1016/j.promfg.2021.06.066.

[40] Wu Y, Perrin M, Pastor ML, Casari P, Gong X. On the determination of acoustic emission wave propagation velocity in composite sandwich structures. Compos Struct 2021;259:113231. https://doi.org/10.1016/j.compstruct.2020.113231.

[41] Pyrzowski Ł, Sobczyk B. Local and global response of sandwich beams made of GFRP facings and PET foam core in three point bending test. Compos Struct 2020; 241:112122. https://doi.org/10.1016/j.compstruct.2020.112122.

[42] Słoński M, Tekieli M. 2D Digital Image Correlation and Region-Based Convolutional Neural Network in Monitoring and Evaluation of Surface Cracks in Concrete Structural Elements. Materials (Basel) 2020;13:3527. https://doi.org/10.3390/ma13163527.